Verification Test Suite for Spalart-Allmaras QCR2000 Turbulence Model

Boris Diskin[1]
National Institute of Aerospace, Hampton, Virginia 23666, USA

Nash'at Ahmad[2], William K. Anderson[3], Joseph M. Derlaga[4], Mohagna J. Pandya[5], Christopher L. Rumsey[6], Li Wang[7], Stephen L. Wood[8]
NASA Langley Research Center, Hampton, Virginia 23681, USA

Yi Liu[9] and Hiroaki Nishikawa[10]
National Institute of Aerospace, Hampton, Virginia 23666, USA

Marshall C. Galbraith[11]
Massachusetts Institute of Technology, Massachusetts 03130, USA

This is an invited paper for the SciTech 2021 special session: High-Fidelity CFD Preworkshop. The paper presents three benchmark cases for verification of Reynolds-averaged Navier-Stokes solvers. The verification studies focus on a one-equation Spalart-Allmaras model that uses a version of quadratic constitutive relations. The benchmark cases are a two-dimensional subsonic flow around a Joukowski airfoil, a three-dimensional supersonic flow through a square duct, and a three-dimensional wing-fuselage junction flow. The turbulence model formulation, geometry, flow conditions, grids, and expected output are described in detail. Reference solutions computed by established and verified codes are shown.

I. Introduction

This paper presents three test cases for verification of Reynolds-averaged Navier-Stokes (RANS) solvers participating in High-Fidelity Computational Fluid Dynamics (CFD) Workshop (HFCFDW). For RANS simulations of corner flows, anisotropy of turbulence stresses can be important because normal stress differences induce flowfield behavior that cannot be captured with linear eddy-viscosity models that make use of the Boussinesq assumption. The verification campaign focuses on RANS solvers with the nonlinear one-equation Spalart-Allmaras Quadratic-Constitutive-Relation (SA-QCR2000) model [1]. The negative variant, SA-[neg]-QCR2000 [2] is recommended.

The cases include a subsonic two-dimensional flow around a Joukowski airfoil, a supersonic flow through a square-duct configuration described in Ref. [3], and a subsonic wing-body juncture flow [4]. Families of consistently refined grids have been generated for each case and made available to the

---

[1]Senior Research Fellow, Associate Fellow AIAA
[2]Research Scientist, Computational Aeroscienses Branch, Senior Member AIAA
[3]Senior Research Scientist, Computational Aeroscienses Branch, Associate Fellow AIAA
[4]Research Scientist, Computational Aeroscienses Branch, Member AIAA
[5]Research Aerospace Engineer, Configuration Aerodynamics Branch, Senior Member AIAA.
[6]Senior Research Scientist, Computational Aeroscienses Branch, Fellow AIAA
[7]Research Aerospace Engineer, Computational Aeroscienses Branch, Associate Fellow AIAA
[8]Research Scientist, Computational Aeroscienses Branch, Member AIAA
[9]Senior Research Scientist, Senior Member AIAA.
[10]Associate Research Fellow, Associate Fellow AIAA
[11]Research Engineer, Department of Aeronautics & Astronautics, Senior Member AIAA

community through NASA Langley Turbulence Modeling Resource (TMR) website[*]. To minimize grid effects on solver verification, HFCFDW participants are required to compute solutions on the grids provided by the workshop. In this paper, reference solutions for each of the three cases are computed using well established RANS solvers to show example computations for workshop participants.

The material in the paper is presented in the following order. The SA-[neg]-QCR2000 turbulence model is described in detail in Section II. Section III briefly introduces solvers used for computing reference solutions. Sections III-V present details of the test cases, describe expected output, and demonstrate reference solutions. Concluding remarks are given in Section VI.

II. Reynolds-Averaged Navier-Stokes Equations with QCR2000 Turbulence Model

Following Ref. [5], the 3D compressible Reynolds-averaged Navier-Stokes equations are given by

$$\partial_t \boldsymbol{Q} + \partial_x \boldsymbol{F} + \partial_y \boldsymbol{G} + \partial_z \boldsymbol{H} = \boldsymbol{0}.$$

Vectors of fluxes $\boldsymbol{F}, \boldsymbol{G}, \boldsymbol{H}$ are defined as

$$\boldsymbol{F} = \begin{pmatrix} \rho u \\ \rho u u + p - \tau_{xx} \\ \rho u v - \tau_{xy} \\ \rho u w - \tau_{xz} \\ (E+p)u - \left(u\tau_{xx} + v\tau_{xy} + w\tau_{xz}\right) + \partial_x q \end{pmatrix},$$

$$\boldsymbol{G} = \begin{pmatrix} \rho v \\ \rho u v - \tau_{xy} \\ \rho v v + p - \tau_{yy} \\ \rho v w - \tau_{yz} \\ (E+p)v - \left(u\tau_{xy} + v\tau_{yy} + w\tau_{yz}\right) + \partial_y q \end{pmatrix},$$

$$\boldsymbol{H} = \begin{pmatrix} \rho w \\ \rho u w - \tau_{xz} \\ \rho v w - \tau_{yz} \\ \rho w w + p - \tau_{zz} \\ (E+p)w - \left(u\tau_{xz} + v\tau_{yz} + w\tau_{zz}\right) + \partial_z q \end{pmatrix}.$$

Here, p is the static pressure, $\boldsymbol{u} = (u, v, w)$ is the velocity vector, and $\boldsymbol{Q} \equiv (\rho, \rho\boldsymbol{u}, E)^T$ is the set of conserved variables that includes the density ρ, the momentum $\rho\boldsymbol{u} = (\rho u, \rho v, \rho w)$, and the total energy per unit volume E. For a perfect gas, the variables are connected through the following relations

$$p = (\gamma - 1)\left(E - \frac{\rho}{2}(u^2 + v^2 + w^2)\right), \qquad a^2 = \gamma\frac{p}{\rho},$$

where a is the speed of sound and $\gamma = 1.4$ is the ratio of specific heats. In this paper, only steady flows are considered. For steady-state RANS equations, the time derivative is dropped. The shear stress tensor and the heat flux vector are defined as

$$\tau_{xx} = \frac{2}{3}\frac{M_{ref}}{Re}(\mu + \mu_t)\left(2\partial_x u - \partial_y v - \partial_z w\right),$$

$$\tau_{yy} = \frac{2}{3}\frac{M_{ref}}{Re}(\mu + \mu_t)\left(2\partial_y v - \partial_x u - \partial_z w\right),$$

$$\tau_{zz} = \frac{2}{3}\frac{M_{ref}}{Re}(\mu + \mu_t)\left(2\partial_z w - \partial_x u - \partial_y v\right),$$

---

[*] https://turbmodels.larc.nasa.gov, Accessed: 2020-**-**

$$\tau_{yx} = \tau_{xy} = (\mu + \mu_t)(\partial_x v + \partial_y u),$$

$$\tau_{zx} = \tau_{xz} = (\mu + \mu_t)(\partial_x w + \partial_z u),$$

$$\tau_{zy} = \tau_{yz} = (\mu + \mu_t)(\partial_z v + \partial_y w),$$

$$\partial_x q = \frac{M_{ref}}{Re(\gamma - 1)}\left(\frac{\mu}{Pr} + \frac{\mu_t}{Pr_t}\right)\partial_x T,$$

$$\partial_y q = \frac{M_{ref}}{Re(\gamma - 1)}\left(\frac{\mu}{Pr} + \frac{\mu_t}{Pr_t}\right)\partial_y T,$$

$$\partial_z q = \frac{M_{ref}}{Re(\gamma - 1)}\left(\frac{\mu}{Pr} + \frac{\mu_t}{Pr_t}\right)\partial_z T.$$

Here, T is the temperature, μ is the dynamic laminar viscosity computed by the Sutherland's law, μ_t is a turbulent eddy viscosity computed by a turbulence model, M_{ref} is the reference Mach number, Re is the Reynolds number, $Pr = 0.72$ and $Pr_t = 0.9$ are the Prandtl number for meanflow and turbulence models, respectively. In the Sutherland's law [6], the local dynamic viscosity is determined by the following formula

$$\mu = \mu_0 \left(\frac{T}{T_0}\right)^{3/2}\left(\frac{T_0 + S}{T + S}\right),$$

where $\mu_0 = 1.716 \times 10^{-5} kg/(ms)$, $T_0 = 491.6°R$, and $S = 198.6°R$.

The standard SA model [7] is given by the following nonconservative equation

$$\partial_t \hat{v} + u\partial_x \hat{v} + v\partial_y \hat{v} + w\partial_z \hat{v} - c_{b1}(1 - f_{t2})\hat{S}\hat{v} + \left[c_{w1}f_w - \frac{c_{b1}}{\kappa^2}f_{t2}\right]\left(\frac{\hat{v}}{d}\right)^2$$
$$- \frac{1}{\sigma}\left[\partial_x\left((v + \hat{v})\partial_x \hat{v}\right) + \partial_y\left((v + \hat{v})\partial_y \hat{v}\right) + \partial_z\left((v + \hat{v})\partial_z \hat{v}\right)\right.$$
$$\left. + c_{b2}\left((\partial_x \hat{v})^2 + (\partial_y \hat{v})^2 + (\partial_z \hat{v})^2\right)\right] = 0.$$

The boundary conditions are

$$\hat{v}_{wall} = 0, \qquad \hat{v}_{farfield} = 3v_{ref}.$$

Here, $\hat{v}$ is the turbulence variable, d is the distance to the nearest wall, $v = \mu/\rho$ is the kinematic viscosity, v_{ref} is the freestream kinematic viscosity.

$$\hat{S} = \Omega + \frac{\hat{v}}{\kappa^2 d^2}f_{v2},$$

where Ω is the magnitude of vorticity,

$$\Omega = \sqrt{\left(\partial_y w - \partial_z v\right)^2 + (\partial_z u - \partial_x w)^2 + \left(\partial_x v - \partial_y u\right)^2},$$

$$f_{v2} = 1 - \frac{\chi}{1 + \chi f_{v1}}, \quad \chi = \frac{\hat{v}}{v}, \quad f_{v1} = \frac{\chi^3}{c_{v1}^3 - \chi^3}, \quad f_w = g\left[\frac{1 + c_{w3}^6}{g^6 + c_{w3}^6}\right]^{\frac{1}{6}}, \quad g = r + c_{w2}(r^6 - r),$$

$$f_{t2} = c_{t3}\exp(-c_{t4}\chi^2), \quad r = \min\left[\frac{\hat{v}}{\hat{S}\kappa^2 d^2}, 10\right],$$

and the constants are

$$\kappa = 0.41, \quad \sigma = \frac{2}{3}, \quad c_{b1} = 0.1355, \quad c_{b2} = 0.622, \quad c_{v1} = 7.1, \quad c_{w1} = \frac{c_{b1}}{\kappa} + \frac{1 + c_{b2}}{\sigma}, \quad c_{w2} = 0.3,$$
$$c_{w3} = 2, \quad c_{t3} = 1.2, \quad c_{t4} = 0.5.$$

To avoid division by zero, the term $\hat{S}$ has to be limited. The particular limiting method used in computations should always be reported. Three limiting methods are recommended:

3

(a) $\hat{S} = \max\left[\Omega + \frac{\hat{v}}{\kappa^2 d^2}, \varepsilon\right]$, where ε is a small positive number;

(b) $\hat{S} = \max\left[\Omega + \frac{\hat{v}}{\kappa^2 d^2}, 0.3\Omega\right]$;

(c) $\bar{S} = \frac{\hat{v}}{\kappa^2 d^2}f_{v2}$, $\hat{S} = \Omega + \bar{S}$ when $\bar{S} \geq -c_2\Omega$; $\hat{S} = \Omega + \frac{\Omega(c_2^2\Omega+c_3\bar{S})}{(c_3-2c_2)\Omega-\bar{S}}$ when $\bar{S} < -c_2\Omega$. In case of zero vorticity ($\Omega = 0$), r is defined explicitly as $r = 10$.

The standard SA model equation is solved for $\hat{v} > 0$. For negative $\hat{v}$, the following equation [2] is solved

$$\partial_t\hat{v} + u\partial_x\hat{v} + v\partial_y\hat{v} + w\partial_z\hat{v} - c_{b1}(1 - c_{t3})\Omega\hat{v} - c_{w1}\left(\frac{\hat{v}}{d}\right)^2$$
$$- \frac{1}{\sigma}\left[\partial_x\big((v + \hat{v}f_n)\partial_x\hat{v}\big) + \partial_y\Big((v + \hat{v}f_n)\partial_y\hat{v}\Big) + \partial_z\big((v + \hat{v}f_n)\partial_z\hat{v}\big)\right.$$
$$\left. + c_{b2}\left((\partial_x\hat{v})^2 + \left(\partial_y\hat{v}\right)^2 + (\partial_z\hat{v})^2\right)\right] = 0$$

with

$$f_n = \frac{c_{n1} + \chi^3}{c_{n1} - \chi^3}, \qquad c_{n1} = 16.$$

The turbulent eddy viscosity is computed as

$$\mu_t = \max\left(\rho\hat{v}f_{v1}, 0\right).$$

For the SA-QCR2000 model [1], the normalized antisymmetric rotation tensor is defined as

$$O_{xy} = -O_{yx} = \frac{\partial_y u - \partial_x v}{b},$$
$$O_{xz} = -O_{zx} = \frac{\partial_z u - \partial_x w}{b},$$
$$O_{yz} = -O_{zx} = \frac{\partial_z v - \partial_y w}{b}.$$

Here, b is the l_2-norm of velocity gradient tensor defined as

$$b = \sqrt{(\partial_x u)^2 + \left(\partial_y u\right)^2 + (\partial_z u)^2 + (\partial_x v)^2 + \left(\partial_y v\right)^2 + (\partial_z v)^2 + (\partial_x w)^2 + \left(\partial_y w\right)^2 + (\partial_z w)^2}.$$

The rotation tensor is set to be zero when $b = 0$. The stress tensor is modified as follows

$$\tau_{xx,QCR} = \tau_{xx} - 2c_{cr1}\big(O_{xy}\tau_{xy} + O_{xz}\tau_{xz}\big),$$
$$\tau_{yy,QCR} = \tau_{yy} - 2c_{cr1}\big(-O_{xy}\tau_{yx} + O_{yz}\tau_{yz}\big),$$
$$\tau_{zz,QCR} = \tau_{zz} - 2c_{cr1}\big(O_{xz}\tau_{zx} + O_{yz}\tau_{zy}\big),$$
$$\tau_{xy,QCR} = \tau_{xy} - c_{cr1}\big(O_{xy}(\tau_{yy} - \tau_{xx}) + O_{yz}\tau_{xz} + O_{xz}\tau_{yz}\big),$$
$$\tau_{xz,QCR} = \tau_{xz} - c_{cr1}\big(O_{xz}(\tau_{zz} - \tau_{xx}) + O_{xy}\tau_{yz} + O_{yz}\tau_{xy}\big),$$
$$\tau_{yz,QCR} = \tau_{yz} - c_{cr1}\big(O_{yz}(\tau_{zz} - \tau_{yy}) - O_{xy}\tau_{xz} - O_{xz}\tau_{xy}\big),$$
$$c_{cr1} = 0.3.$$

III. Computational Fluid Dynamics Codes

This section describes the well-established practical CFD codes used in this study. The codes developed and supported by NASA are widely used by U.S. government, industry, and academia and represent the state of the art in aerodynamic computations.

A. USM3D

USM3D is a cell-centered finite-volume unstructured-grid RANS solver [8] that has been widely used for configuration aerodynamic research within NASA [9], [10] and for product development within major

airframe companies [11]-[13]. The enhanced mixed-element version of USM3D [14]-[17] is used in this study. Mixed-element USM3D solves the governing flow equations on grids composed of tetrahedra, pyramids, prisms, and hexahedra. A fully-implicit formulation is implemented implying that the auxiliary solution variables at the grid nodes and boundary faces as well as the cell gradients are computed solely from the current solution variables defined at the cell centers. Solution values at the nodes are averaged from the solution values at surrounding cells. The second-order spatial discretization of inviscid fluxes is accomplished by reconstructing solutions at the cell faces; the reconstruction is based on solution gradients computed within cells. The reconstruction scheme corresponds to the UMUSCL (Unstructured Monotonic Upstream-centered Scheme for Conservation Laws) scheme [18]-[21] with $\kappa = 0$. The cell gradients are evaluated with the Green-Gauss integration. Inviscid fluxes are computed at each cell face with the upwind Roe's flux-difference-splitting (FDS) scheme. Face gradients required for evaluation of viscous fluxes are computed from the Mitchell stencil [22], [23]. The convection term of the SA turbulence model equation is approximated with first-order accuracy. The velocity gradients contributing to the source term of the SA model are computed at cell centers as the face area average of face gradients.

B. FUN3D-FV

FUN3D-FV is a node-centered finite-volume unstructured-grid RANS solver developed and supported at NASA LaRC, which is widely used for high-fidelity analysis and adjoint-based design of complex turbulent flows [24], [25]. Recently FUN3D-FV has been successfully ported on advanced computing architectures♦ [26]. FUN3D-FV solves the governing flow equations on mixed-element grids. At median-dual control-volume faces, the inviscid fluxes are computed using an approximate Riemann solver. Roe's FDS scheme is used in the current study. For second-order accuracy, face values are obtained by a UMUSCL scheme, with unweighted least-squares gradients computed at the nodes. For this study, the UMUSCL scheme with $\kappa = 0.5$ is used for the meanflow equations.

The viscous fluxes use full approximation of viscous stresses and heat fluxes. For tetrahedral meshes, the viscous fluxes are discretized using the Green-Gauss (cell-based) gradients; this is equivalent to a Galerkin type approximation. For nontetrahedral meshes, the edge-based gradients are combined with Green-Gauss gradients; this improves stability of the viscous operator. The diffusion term in the turbulence model is handled in the same fashion as the meanflow viscous terms. In these studies, FUN3D-FV uses a first-order approximation for the convection term in the turbulence-model equation.

C. FUN3D-SFE

SFE is a stabilized finite-element discretization recently added as a library to FUN3D [27]. The implementation supports the same element types as the FUN3D-FV scheme and high-order spatial discretizations. The turbulence model equation is discretized in the same way as the meanflow equations. As a result, the FUN3D-SFE discretization of the RANS equations is fully second order. The formulation includes a combination of a discretization based upon the streamlined upwind Petrov-Galerkin scheme and penalty terms to enforce boundary conditions and to capture shocks.

D. OVERFLOW

OVERFLOW is a structured, overset-grid RANS solver widely used across NASA and industry [28]. Both finite-volume and finite-difference discretizations of first through fifth order for the inviscid fluxes and second order for viscous fluxes are available in the interior; there are first- through third-order inviscid fluxes for the turbulence model as well. Overset interpolation is based on trilinear interpolation.

E. SANS

Solution Adaptive Numerical Simulator (SANS) [29], currently under development at the Massachusetts Institute of Technology, is a general framework for solving discrete finite-element approximations to advection-diffusion-reaction type PDEs, such as scalar advection-diffusion, Navier-Stokes, and RANS

♦ https://blogs.nvidia.com/blog/2019/11/18/nasa-mars-landing-simulation-gpus/

equations. A range of finite-element methods are currently implemented in SANS, including high-order discontinuous (DG), hybridized discontinuous (HDG), and continuous (CG) Galerkin finite-element methods. The Variational Multiscale Method with Discontinuous Subscales (VMSD) [30], [31] discretization is used to compute all solutions to the RANS equations presented here. Boundary conditions are weakly enforced, and forces are computed using the residual balance at the boundary.

The nonlinear system of equations is solved using pseudotime continuation (PTC) damped Newton's method with a line search to ensure that residuals decrease. The complete linearization of the residual is computed via operator overloaded automatic differentiation [32]. The PTC algorithm computes an element local time step based on the characteristic speed, element size, and a Courant-Friedrichs-Lewy (CFL) number. The inverse CFL is driven toward zero such that a Newton-like convergence rate is recovered. The Portable, Extensible Toolkit for Scientific Computation (PETSc) [33]-[35] framework is used to solve the linear system for each PTC iteration with restarted generalized minimal residual (GMRES) [36] preconditioned with an Incomplete Lower Upper (ILU) factorization. Parallel computations use the restricted additive Schwarz preconditioner with three layers of overlap. The ILU preconditioner is applied to each subdomain, and restarted GMRES is applied to the global system. Adjoint systems are solved using the same linear solver as the primal. All discrete solutions are converged to near machine-zero residuals.

IV. Test Case 1: Joukowski Airfoil

This test case is designed as a verification case for the SA-[neg]-QCR2000 RANS equations where the theoretical optimal convergence rates in drag error are observable. The Joukowski airfoil, shown in Fig. 1, is used for this test as the cusped trailing edge removes the inviscid singularity at the trailing edge at zero degrees angle of attack. However, there is still a singularity in skin friction. Two families of grids will be presented here where nodes are clustered at both the trailing edge singularity and the stagnation point in order to capture the expected order of accuracy. The "Classic" family of grids is a structured set of grids that follow classic meshing guidelines with gradual grid lines near orthogonal to the geometry and low element size ratios. The "Challenge" family of grids is skewed at the geometry and has large element size ratios to stress the robustness of a solver with respect to grid quality.

For this test case, the freestream Mach number is 0.5, the Reynolds number is 1,000,000 based on chord, the angle of attack is 0 degrees, and the heat capacity ratio is $\gamma = Cp/Cv = 1.4$. A freestream value of $v_t/v = 3$ is used for the SA turbulence model. The final paper will present and discuss reference solutions computed using established CFD codes.

The optimal convergence rate in drag error is 2P for an adjoint consistent discretization, where P represents the polynomial degree in a finite element discretization or the reconstruction polynomial degree in a finite volume discretization. Without adjoint consistency, the convergence rate should be at least P+1.
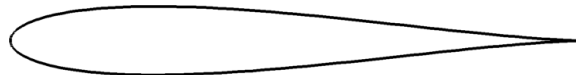

Fig. 1 Joukowski airfoil geometry.

V. Test Case 2: Supersonic Flow through Square Duct

A. Geometry, Flow, and Boundary Conditions

This test case studies a supersonic flow through a long duct with a square cross-section of height and width $D = 25.4mm$. The configuration geometry and boundary conditions are illustrated in Fig. 2. The experimental measurements were conducted at the stations located $40D$ and $50D$ downstream of the duct inlet. The origin of the coordinate system is set at the lower-left corner of the front section of the duct. The positive direction of the x-axis is the streamwise direction along the duct. The duct dimensions are $0 \leq x \leq 52D; 0 \leq y \leq 0.5D; 0 \leq z \leq 0.5D$. Adiabatic-wall conditions are set at the duct boundaries corresponding to $0 \leq x \leq 52D; y = 0; 0 \leq z \leq 0.5D$ and $0 \leq x \leq 52D; 0 \leq y \leq 0.5D; z = 0$. The computational

domain is extended upstream with a small segment of symmetry boundaries $-1.26829D \leq x \leq 0$. The flow corresponds to the reference freestream Mach number $M_\infty = 3.9$, the Reynolds number $Re_D = 5.08 \times 10^5$, the angle of attack $\alpha = 0°$, and the reference freestream temperature $T_\infty = 520°R$ Supersonic inflow conditions are set at $x = -1.26829D$ corresponding to the reference conditions. Supersonic outflow conditions are set at $x = 52D$. Symmetry conditions are also specified at the boundaries corresponding to $y = 0.5D$, and $z = 0.5D$, thus, only one quarter of the duct is computed. The reference area is unity.
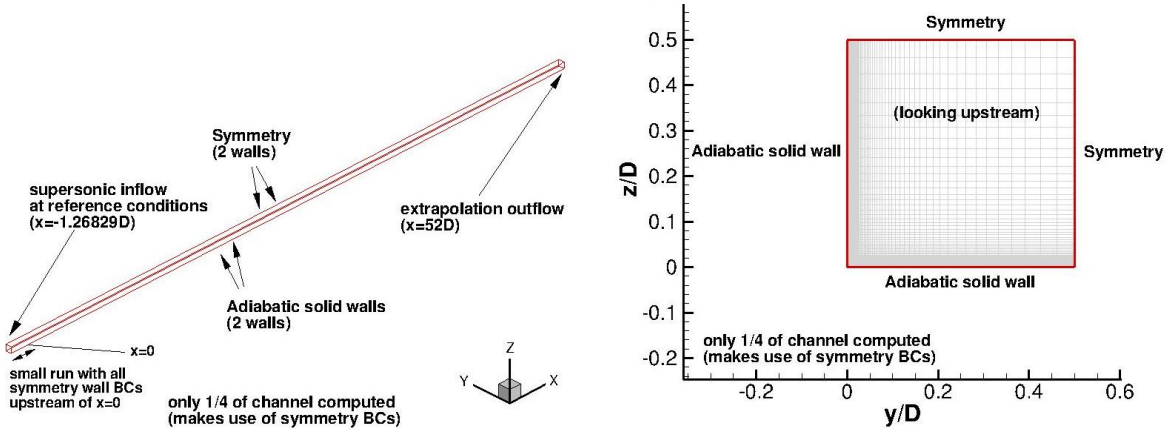
Fig. 2 Geometry and boundary conditions.

B. Grids

A family of hexahedral grids has been generated using a FORTRAN programs available at the TMR website under the "Cases and Grids for Turbulence Model Numerical Analysis" section, "3D Modified Supersonic Square Duct Validation Case" subsection. Due to the use of symmetry boundary conditions, only one quarter of the duct is computed. Grid family includes nested hexahedral grids. Table 1 provides grid statistics for the four finest grids in the family. The grids are stretched in the wall-normal directions with a constant stretching factor. A mild streamwise stretching is applied within the duct to improve grid smoothness. Grid 1 has 2688 cells in the streamwise direction and 768 cells in the spanwise and vertical directions, the minimum nondimensional spacing at the wall of approximately 0.0000085, and the average $y^+ = 0.022$.

Table 1 Family of hexahedral grids for square duct.

Grid	Cells	Nodes
4	3,096,576	3,170,833
3	24,772,608	25,068,577
2	198,180,864	199,362,625
1	1,585,446,912	1,590,169,729

C. Optional Setting

The setting with the upstream symmetry run and without downstream symmetry run is the main setting for which the reference solutions have been produced. However, an optional setting can be used as long as the produced solutions do not deviate from the reference solutions. The grid generation code can generate grids with and without symmetry runs upstream and downstream of the duct. The run of symmetry boundary can be added downstream of the duct $52D \leq x \leq 53.268290D$. In this optional setting, supersonic outflow is set at $x = 53.268290D$ and symmetry conditions are used on all boundaries at $52D \leq x \leq 53.268290D$. In preliminary computations conducted with FUN3D-FV and USM3D, the presence of the downstream symmetry run had no noticeable effects on the computed solutions within the duct, but significantly increased computational time to converge residuals to the machine-zero level.

D. Summary of Input Parameters

FUN3D-FV and USM3D solvers compute reference solutions for the supersonic flow through the square duct. The following input parameters are used:

- Unit length: $D = 1$.
- Length of duct: $L = 52$.
- Width and height of duct: $D = 1$.
- Reynolds number per unit length: $Re_D = 508,000$.
- Reference freestream Mach number: $M_\infty = 3.9$.
- Reference freestream temperature: $T_\infty = 520°R$.
- Reference area: $A_\infty = 1$.
- Meanflow inviscid terms: Roe's FDS, second order, no limiters.
- Gradients for inviscid reconstruction: USM3D uses Green-Gauss gradients based on nodal solutions; FUN3D uses unweighted least-squares method.
- Meanflow viscous terms: Full Navier-Stokes, second order.
- Gradients for viscous terms: USM3D uses Mitchell's method; FUN3D uses cell-based Green-Gauss method with edge-based augmentation.
- Turbulence model: SA-neg-QCR2000.
- Clipping method for $\hat{S}$: USM3D uses method "a" with cut-off 0.00001; FUN3D uses method "c".
- Dynamic viscosity: Sutherland's law
- SA-model diffusion term: Full Navier-Stokes, second order.
- SA-model advection term: Nonconservative upwind approximation [2], first order.
- SA-model variable in farfield: $\hat{v}_{farfield} = 3 \times$ freestream laminar kinematic viscosity.
- Prandtl number for diffusion fluxes: 0.72 for meanflow, 0.90 for SA model.
- Initial conditions: Based on reference freestream conditions.

E. Output Requirements

All solvers participation in HFCFDW are required to report residual convergence on all grids. It is recommended to show residual convergence history versus iterations and/or CPU time. Contour plots of the cross-stream velocity normalized by the reference freestream speed of sound (a_∞) should be shown for visual solution inspection. Secondary circulation is expected to be clearly observed.

Grid convergence of the following scalar quantities should be reported:
- Drag coefficient computed over the solid-wall boundary.
- Centerline velocity normalized by the reference speed of sound (u/a_∞) at $x/D = 40$ and $x/D = 50$.

Grid convergence of the following line plots should be reported:
- Centerline velocity normalized by the reference speed of sound (u/a_∞) versus x/D.
- Skin-friction coefficient versus $2z/D$ at $x/D = 40$ and $x/D = 50$.
- Vertical and diagonal cuts of the streamwise velocity normalized by the reference speed of sound (u/a_∞) versus $2z/D$ at $x/D = 40$ and $x/D = 50$. For comparison with the experimental data (Ref. [3]), the streamwise velocity should be normalized by the cross-sectional centerline velocity.

F. Reference Solutions

Reference solutions for the supersonic flow through the square duct are computed by USM3D and FUN3D-FV solvers. The computations are different from results reported in Ref. [28] for the same configuration and flow conditions. The finest grid generated for the current computations is 64 times bigger and provides approximately 1.6 billion degrees of freedom; all coarser grids in the family are derived by

consistent (nested) coarsening of the previous finer grid. Also, the implementation of the adiabatic-wall boundary condition in these FUN3D-FV solutions has been changed. The previous implementation relied on a constant-temperature approximation to the adiabatic condition, which is not well-suited for high-speed flows. The current genuine implementation of the adiabatic-wall condition uses zero heat flux through the boundary and results in much better agreement between FUN3D-FV and USM3D solutions. The improved code-to-code comparison is credited to the rigor of the current solver verification exercise.

USM3D computes solutions on the four finest grids shown in Table 1 and FUN3D-FV computes solutions on grids 2, 3, and 4. In the final paper, FUN3D solutions on the finest grid will be shown as well. All solutions converge the root-mean square norm of residuals to the levels below 10^{-13}. Table 2 shows the drag coefficient, maximum eddy viscosity, and the centerline velocity computed on the two finest grids. The centerline velocity is shown at two locations, $x/D = 40$ and $x/D = 50$, and normalized by the freestream speed of sound (a_∞) and maximum eddy viscosity normalized by the freestream laminar viscosity (μ_∞).

Table 2 Drag, maximum eddy viscosity, and centerline velocity computed on Grid 2 and Grid 1.

Solver, Grid	Drag Coefficient	Maximum Eddy Viscosity (μ_t/μ_∞)	Centerline Velocity (u/a_∞)	
			$x = 40$	$x = 50$
USM3D, Grid 1	0.09567343	1660.3208	3.4205277	3.0154017
USM3D, Grid 2	0.09568115	1659.2053	3.4201688	3.0150415
FUN3D-FV, Grid 2	0.09547659	1659.4202	3.4172101	3.0117500

Figure 3 shows grid convergence of the drag coefficient and the maximum eddy viscosity versus the nominal mesh size computed as $h = N^{-1/3}$, where N is the number of degrees of freedom, cells for USM3D and nodes for FUN3D-FV. The drag coefficients computed with USM3D and FUN3D-FV appear converging to the same limit in grid refinement. USM3D drag converges with an apparent order higher than first, FUN3D-FV drag convergence appears as first order. The maximum eddy viscosity plots are almost straight lines indicating first-order convergence. Figure 4 shows grid convergence of centerline velocity normalized by the freestream speed of sound at two locations, $x/D = 40$ and $x/D = 50$. The qualitative and quantitative agreement between USM3D and FUN3D-FV solutions is much superior to the agreement observed in Ref. [28]. In the later reference, the centerline velocities did not converge monotonically in grid refinement and tended to different limits. In the current computations, convergence is monotonic and plots appear approaching the same limit. The quantitative difference between the two plots is also significantly reduced: drag coefficients computed on Grid 2 (about 200M degrees of freedom) differ by about 2 counts; the difference on Grid 1 is expected to be less than 0.2%.
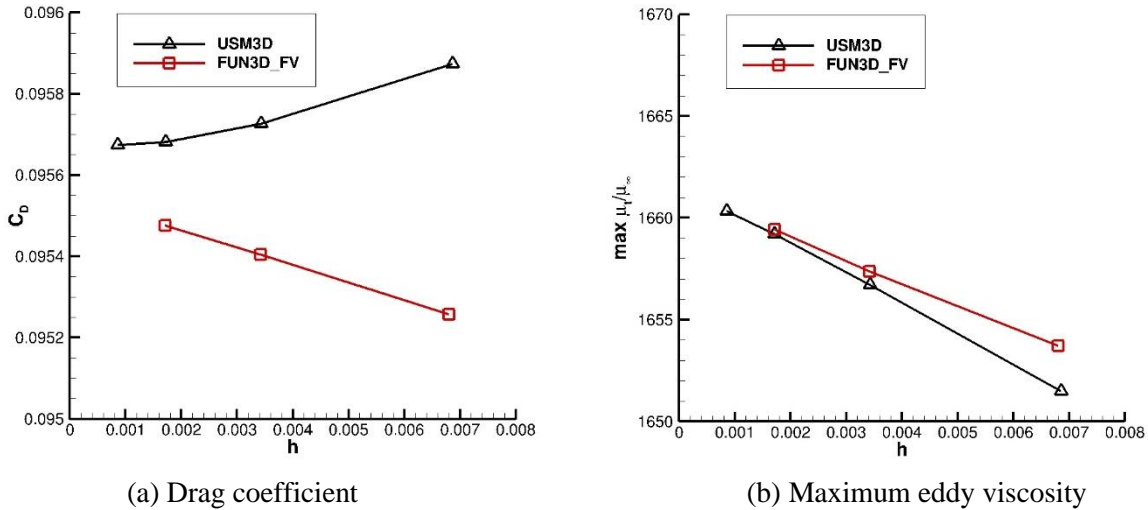

(a) Drag coefficient   (b) Maximum eddy viscosity

Fig. 3 Grid convergence of drag and maximum eddy viscosity.

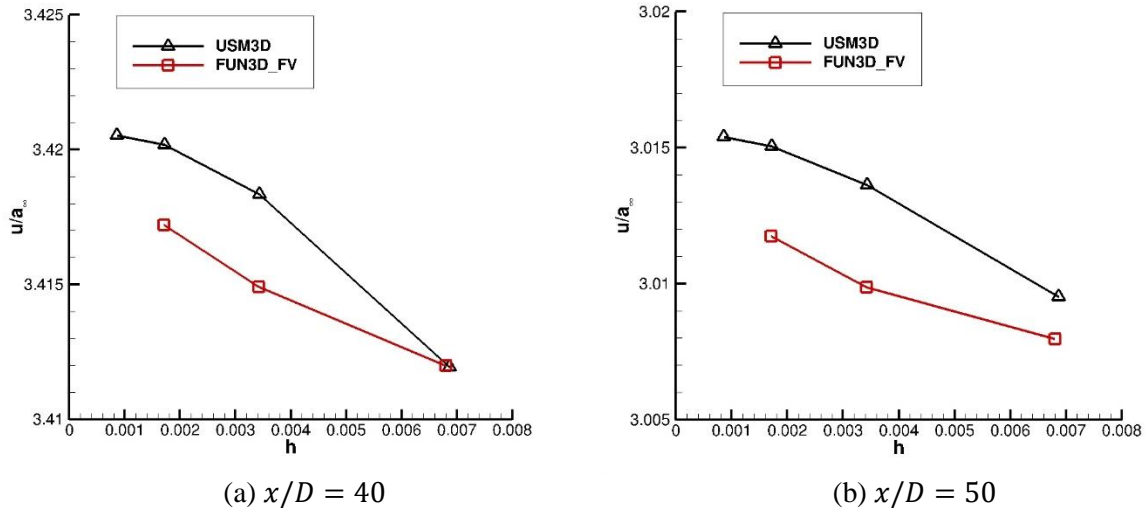(a) $x/D = 40$ (b) $x/D = 50$

Fig. 4 Grid convergence of centerline velocity.

Figure 5 exhibits the line plots of the centerline velocity computed on Grid 2. A shock train is clearly visible in the global view shown in Fig. 5(a). Recall that the computations are done without gradient limiters, which explains the numerical oscillation occurring behind shocks in the forward part of the supersonic duct. Although not shown, the shock position and the levels of centerline velocity are well established in grid refinement. Solutions computed by the two codes are hardly distinguishable outside of the narrow regions around shocks even in the zoomed view shown in Fig. 5(b). The numerical oscillations are not visible for $x/D > 20$. Figures 6(a) and 6(b) illustrate grid convergence of the centerline velocity in the interval $20 < x/D < 35$. Excellent grid convergence is observed.

(a) Global view   (b) Zoomed view
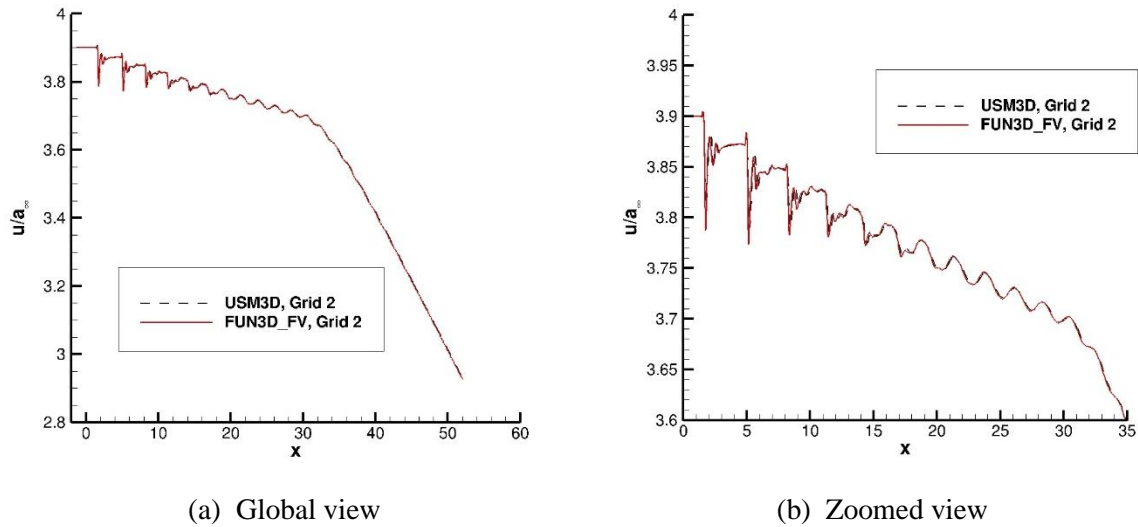
Fig. 5 Centerline velocity computed on Grid 2.

10

(a) USM3D

(b) FUN3D-FV
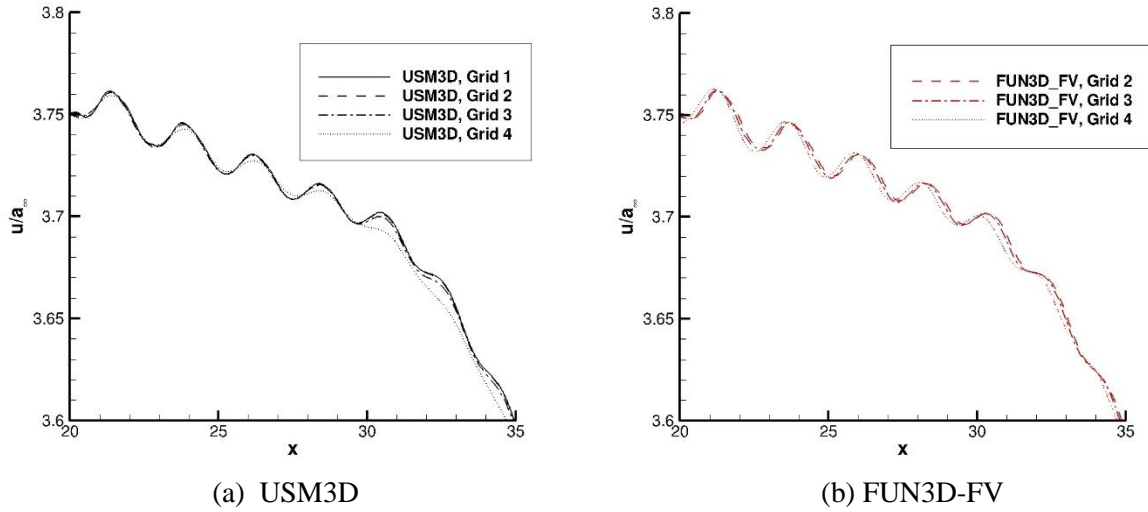
Fig. 6 Grid convergence of centerline velocity, zoomed view.

Figure 7 shows the variation of the streamwise velocity along the diagonal cut ($y = z$) and along the vertical cut ($y/D = 0.5$) at two cross-sections corresponding to $x/D = 40$ and $x/D = 50$. Excellent grid convergence is observed. The velocity profiles computed on all grids overplot in the global views. Variation of the streamwise velocity compares well with experimental data digitized from Ref. [3]. The computational and experimental data are normalized by the centerline velocity in the corresponding cross-section.

(a) Diagonal cut at $x/D = 40$

(b) Vertical cut at $x/D = 40$
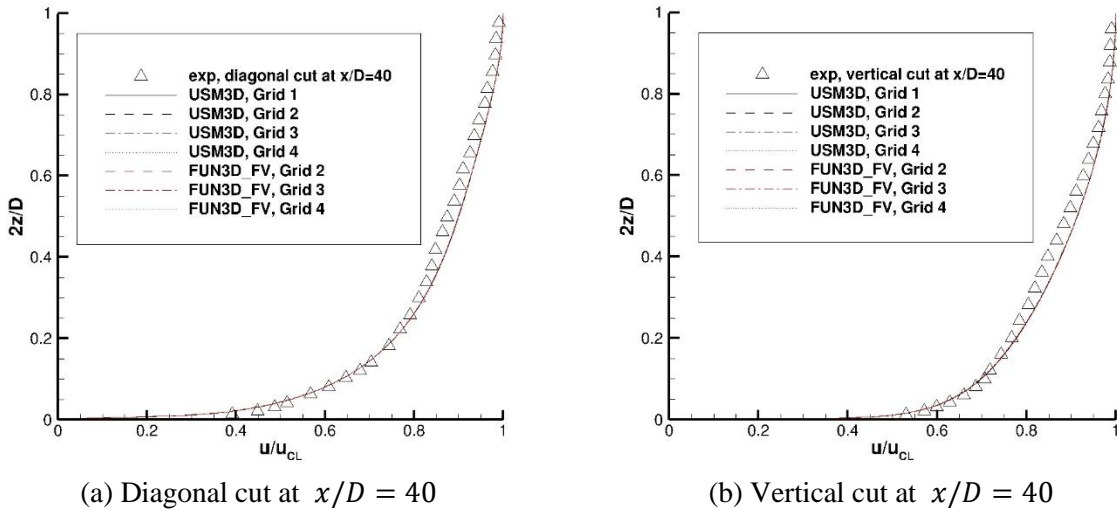
Fig. 7 Variation of streamwise velocity.
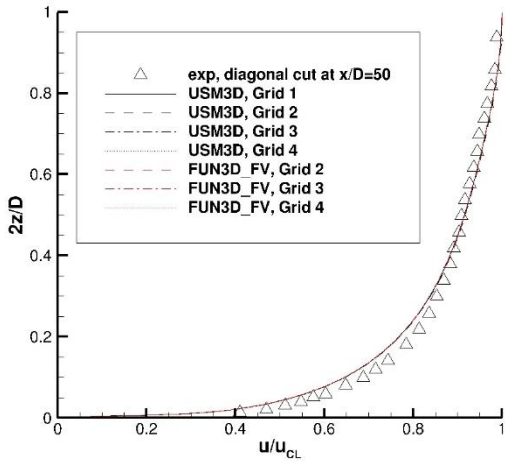
(c) Diagonal cut at $x/D = 50$ (d) Vertical cut at $x/D = 50$
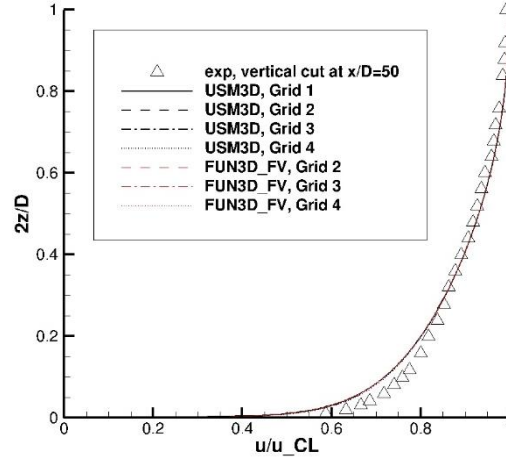
Fig. 7 Concluded.

Figures 8 and 9 illustrate variation of the skin friction coefficient along the *z*-direction at $x/D = 40$ and $x/D = 50$, respectively. Again, excellent grid convergence is observed. The skin-friction coefficients computed on the two finest grids are barely distinguishable even in a zoomed view. A good agreement with experiment is evident. The skin-friction experimental data are inferred from Ref. [3]. In the report, the skin-friction data are given in terms of edge variables. To plot the experimental data normalized with respect to the freestream reference quantities, the following ratios are used $u_{edge}/u_{ref} = 0.856, (\rho u)_{edge}/(\rho u)_{ref} = 1.7$ at $x/D = 40$ and $u_{edge}/u_{ref} = 0.728, (\rho u)_{edge}/(\rho u)_{ref} = 1.4$ at $x/D = 50$.
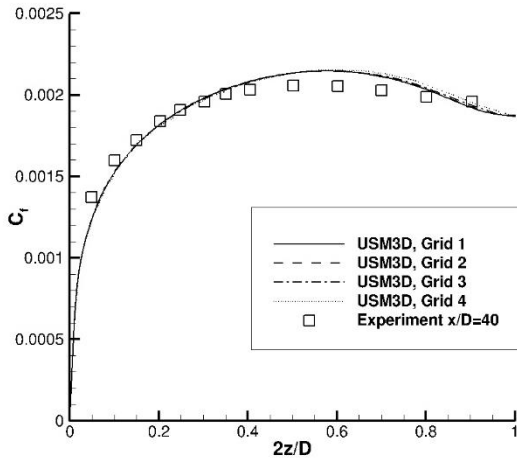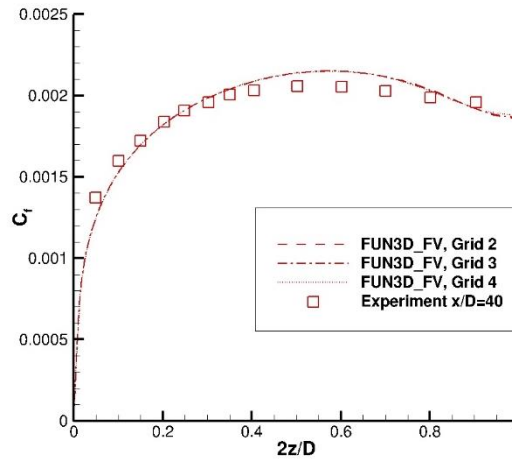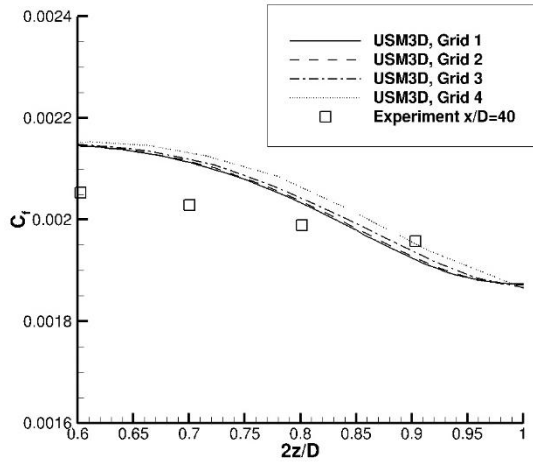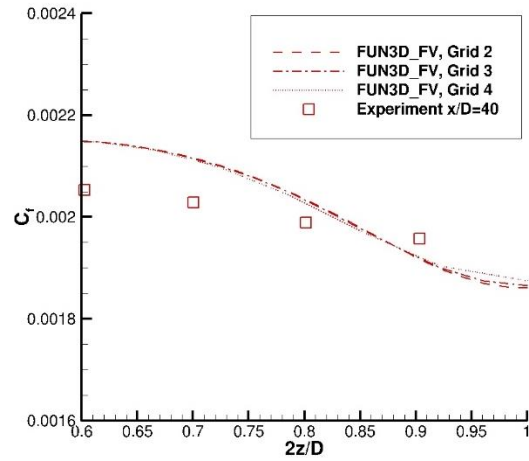

(a) USM3D, global view   (b) FUN3D-FV, global view

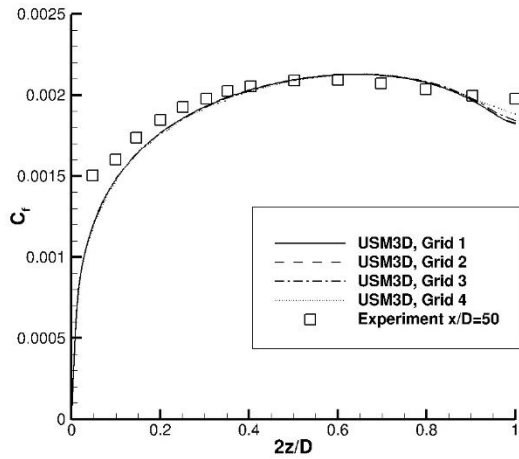**Fig. 8 Variation of skin-friction coefficient at $x/D = 40$.**
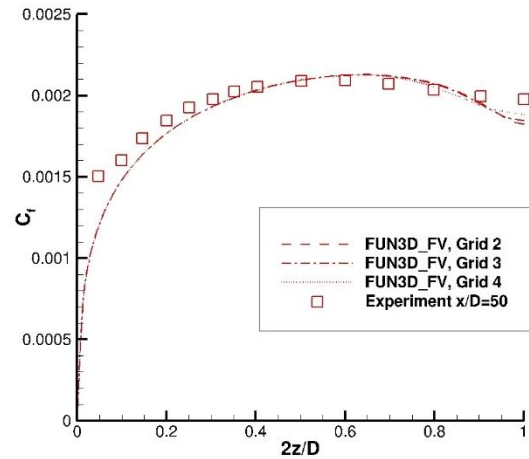
12

(c) USM3D, zoomed view   (d) FUN3D-FV, zoomed view

Fig. 8 Concluded.

(a) USM3D, global view   (b) FUN3D-FV, global view

Fig. 9 Variation of skin-friction coefficient at $x/D = 50$.

(c) USM3D, zoomed view
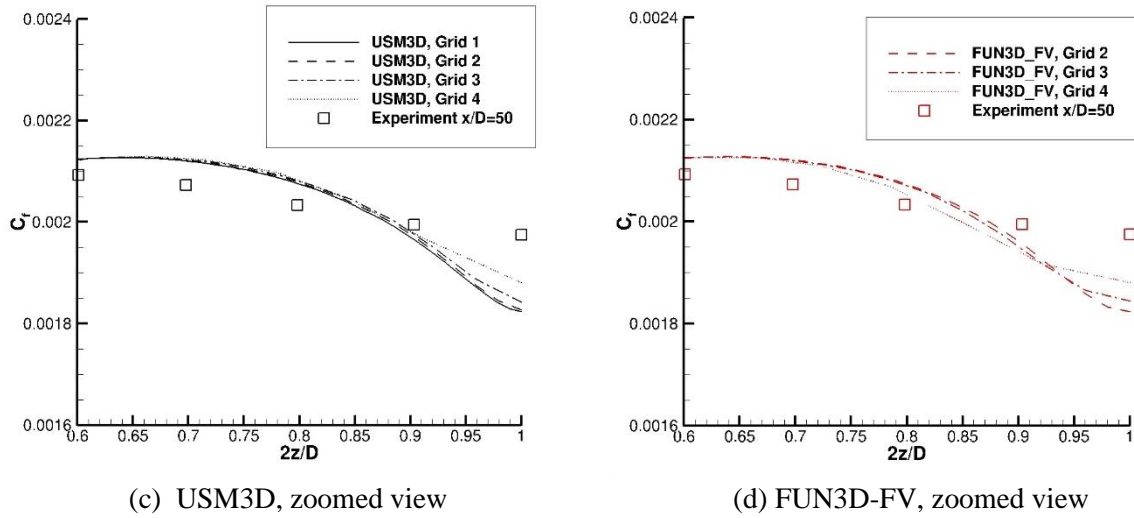
(d) FUN3D-FV, zoomed view

Fig. 9 Concluded.

Figure 10 shows the contours of the crossflow velocity normalized by the reference speed of sound ($\sqrt{v^2 + w^2}/a_{inf}$) and computed at $x/D = 50$. USM3D solution is computed on the finest grid with 1.6 billion cells; the FUN3D-FV solution is computed on the second finest grid with about 200 million nodes. The SA-QCR2000 solution clearly exhibits secondary circulation that cannot be captured with Boussinesq turbulence models. The maximum crossflow velocity in the USM3D solution is 0.0367476.
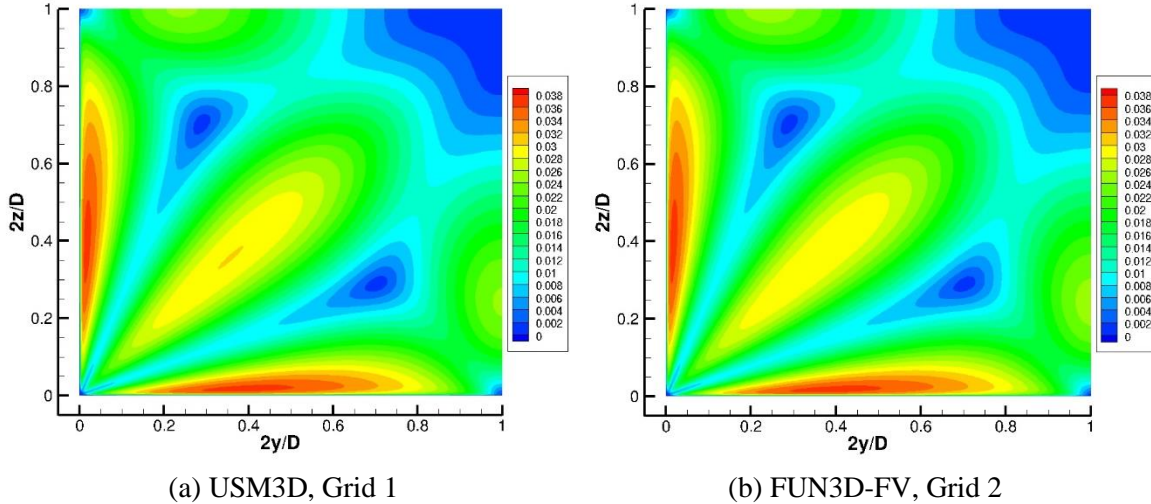

(a) USM3D, Grid 1

(b) FUN3D-FV, Grid 2

Fig. 10 Crossflow velocity at $x/D = 50$.

VI.   Test Case 3: Juncture Flow

A.   Juncture-Flow Experiment: Geometry, Flow, and Boundary Conditions

The NASA juncture-flow experiment was conducted in the NASA Langley Research Center 14-by-22-Foot Subsonic Tunnel. The model was a full-span wing-fuselage body that was configured with truncated DLR-F6 wings, both with and without leading-edge extensions at the wing root. Figure 11 illustrates the model geometry. The model had a fuselage length of $4.839\ m$ with a wingspan of $3.397\ m$ (tip to tip). The wing had a leading edge sweep of 27.1°.

The coordinate system origin $(x, y, z) = (0, 0, 0)$ is placed at the model nose with the x-axis running downstream along the center axis of the fuselage, z-axis is up, and y-axis points out of the starboard wing. The fuselage had flat sides at $y = \pm 236.098 \, mm$. The wing trailing edge at the root was at $x = 2961.929 \, mm$. A half model can be used in CFD simulations to reduce computational cost.
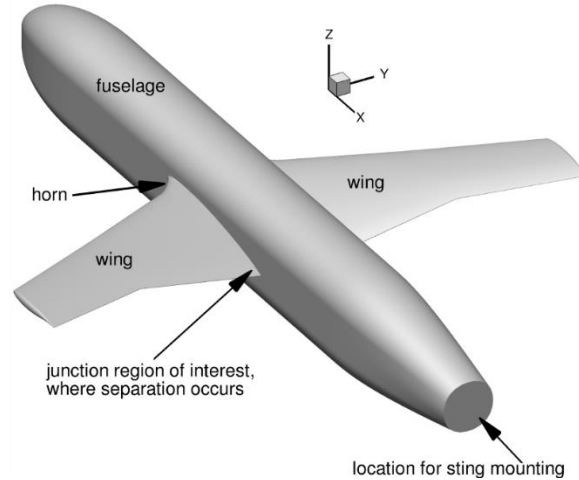

Fig. 11 Juncture-flow model geometry.

The experiment provides flowfield data (velocity, Reynolds stresses, and velocity triple products) in the vicinity of the wing-body junction. The experiment was designed for validating CFD solutions predicting flows in corner regions. The flow physics of wing-body juncture flows is quite complex [38], [39]. In addition to the typical presence of a horseshoe vortex wrapping around the wing leading edge, there also may be a smaller secondary corner vortex initiated by gradients of the Reynolds stresses [40]. These vortices influence the flowfield in the junction region.

The model was tested at a fixed chord Reynolds number of 2.4 million, and angles-of-attack ranging from -10 degrees to +10 degrees were considered. Flowfield measurements were performed with a pair of miniature laser Doppler velocimetry (LDV) probes that were housed inside the model and attached to three-axis traverse systems. One LDV probe was used to measure the separated flow in the trailing-edge junction region. The other LDV probe was alternately used to measure flow velocity in the leading-edge region of the wing and to measure the incoming fuselage boundary layer well upstream of the leading edge. Both LDV probes provided measurements from which all three mean velocity components, all six independent components of the Reynolds-stress tensor, and all ten independent components of the velocity triple products were calculated. In addition to the velocity measurements, static and dynamic pressures were measured at selected locations on the wings and fuselage of the model, infrared imaging was used to characterize boundary-layer transition, oil-flow visualization was used to visualize the separated flow in the leading- and trailing-edge regions of the wing, and unsteady shear stress was measured at several locations using capacitive shear-stress sensors.

Comparison of the computational and experimental data for the juncture flow conditions has been the focus of recent publications and special sessions. The reported computational models include RANS models [41]-[45], hybrid models [46], wall modeled large-eddy simulations [47], [48], and lattice-Boltzmann very large eddy simulations [49]. The first HFCFDW focuses on verification of a specific RANS model, SA-[neg]-QCR2000, for this juncture flow. For the workshop computations, a leading edge fillet or horn is included on the wing to mitigate the formation of a strong horseshoe vortex. The following flow conditions are set: the freestream Mach number is 0.189, a Reynolds number of 2.4 million based on crank chord of ($557.17 \, mm$), the angle of attack of 5°, the heat capacity ratio is $\gamma = 1.4$, and the reference temperature is 519.92ºR. The dynamic viscosity is modeled using Sutherland's law. The meanflow Prandtl number is $Pr = 0.72$, and the turbulent Prandtl number of $Pr_t = 0.9$. For the SA turbulence model, the SA

variable in the farfield is set as $\hat{v}_{farfield} = 3 \times$ freestream laminar kinematic viscosity. For force calculations, the reference area is $965543.2302\ mm^2$ (semispan model).

The farfield boundary can be modelled with a Riemann invariant or characteristic boundary condition. The wing and fuselage surfaces are assigned with a no-slip adiabatic-wall boundary condition. Symmetry boundary condition is imposed at the x-z plane located on the centerline of the fuselage.

B. Grids
In the final paper, CFD grids will be described here.

C. Output Requirements
All solvers participating in HFCFDW are required to compute solutions on the workshop provided grids and report residual convergence on all grids. It is recommended to show residual convergence history versus iterations and/or CPU time.

Grid convergence of lift and drag coefficients computed over the adiabatic-wall boundary should be reported. Preliminary CFD simulations on a refined grid indicate $C_L \approx 0.85$ and $C_D \approx 0.07$. Grid convergence of pressure coefficient at three locations should be reported. The pressure coefficients variation over the wing should be reported in three x-z planes corresponding to $y = -254mm, y = -290.83mm$, and $y = -1663.7mm$. The locations coincide with the experimental measurement locations shown in Figure 12. Pressure contours are shown on the model surface.
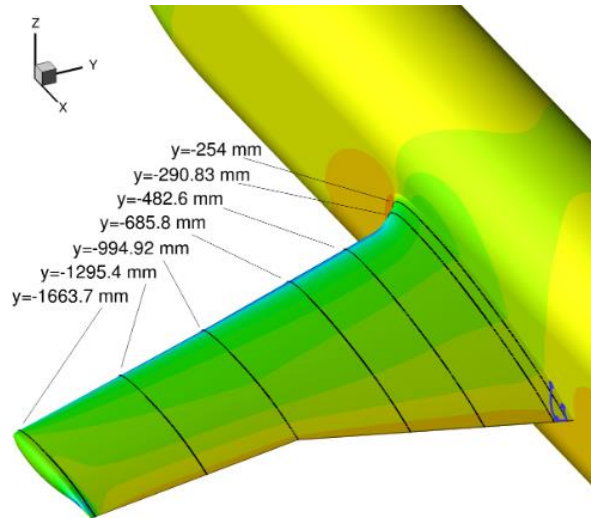

Fig. 12 Locations of wing pressure measurements. Participants only need to report C_P at three locations ($y = -254mm, y = -290.83mm$, and $y = -1663.7mm$).

On this configuration, flow separation occurs near the wing upper surface trailing edge, at the wing-fuselage juncture. Workshop participants should provide the x-coordinate of the apex of this separation. The apex is defined as the point on the wing-fuselage intersection where a surface streamline deviates in the spanwise direction along the foremost edge of the separated region. At this location, the x-component of the skin friction changes sign from positive to negative. A typical result might be $x \approx 2810mm$.

In addition, workshop participants should show variation of velocity components, turbulent normal stresses, and turbulent shear stresses along four lines detailed in Table 3 and depicted in Figure 13. The three components of velocity should be nondimensionalized by the freestream flow speed, $U_\infty: u_i/U_\infty$. The six components of turbulent Reynolds stresses should be nondimensionalized by $U_\infty^2: \overline{u_i'u_j'}/U_\infty^2$.

Table 3 Flow profile lines.

Profile	Line	$x(mm)$	$y(mm)$	$z(mm)$
1	from	1168.4	Surface (≈ -236.1)	0.0
	to	1168.4	-300.0	0.0
2	from	2747.6	-237.1	Surface (≈ 16.75)
	to	2747.6	-237.1	130.0
3	from	2852.6	-237.1	Surface (≈ -8.46)
	to	2852.6	-237.1	130.0
4	from	2852.6	-266.1	Surface (≈ -3.68)
	to	2852.6	-266.1	130.0

(a) Profile 1   (b) Profile 2   (c) Profile 3   (d) Profile 4
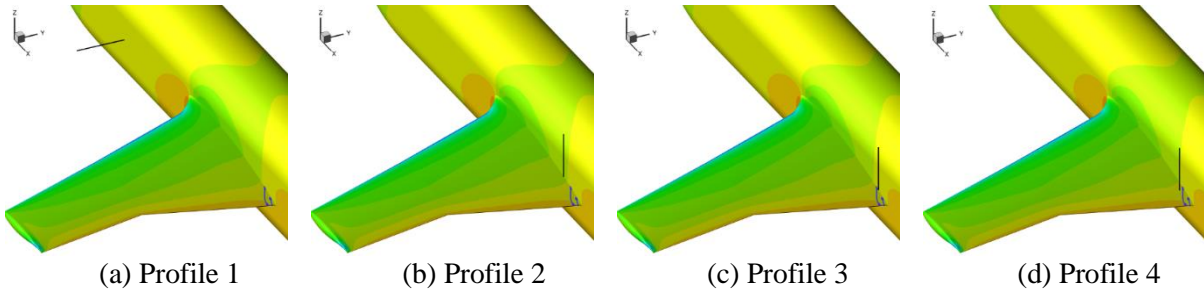
Fig. 13 Locations of flow profile lines detailed in Table 3.

D. Reference Solutions

In the final paper, reference solutions for the junction flow test case computed with established and verified CFD codes will be shown here.

VII. Concluding Remarks

Summary of the reference solutions will be given here in the final paper.

Acknowledgments

References

[1] Spalart, P. R., "Strategies for Turbulence Modelling and Simulation," *International Journal of Heat and Fluid Flow*, Vol. 21(3), 2000, pp. 252-263.

[2] Allmaras, S. R., Johnson, F. T., and Spalart, P. R., "Modifications and Clarifications for the Implementation of the Spalart-Allmaras Turbulence Model," Seventh International Conference on Computational Fluid Dynamics, Big Island, Hawaii, 2012.

[3] Davis, D. O. and Gessner, F. B., "Further Experiments on Supersonic Turbulent Flow Development in a Square Duct," *AIAA Journal*, Vol. 27, No. 8, 1989, pp. 1023-1030

[4] Kegerise, M. A. and Neuhart, D. H., "An Experimental Investigation of a Wing-Fuselage Junction Model in the NASA Langley 14- by 22-Foot Subsonic Tunnel," NASA TM–2019-220286, June 2019

[5]   Biedron R.T., Vatsa V.N., Atkins H.L., "Simulation of Unsteady Flows Using an Unstructured Navier-Stokes Solver on Moving and Stationary Grids," AIAA Paper 2005-5093.

[6]   White, F. M., "Viscous Fluid Flow," McGraw Hill, New York, 1974, p. 28

[7]   Spalart, P. R. and Allmaras, S. R., "A One-Equation Turbulence Model for Aerodynamic Flows," *Recherche Aerospatiale*, No. 1, 1994, pp. 5-21.

[8]   Pandya, M. J., Frink, N. T., Abdol-Hamid, K. S., Samareh, J. A., Parlette, E. B., and Taft, J. R., "Enhancements to TetrUSS for NASA Constellation Program," *Journal of Spacecraft and Rockets*, Vol. 49, No. 4, 2012, pp. 617-631. doi: 10.2514/1.A32089

[9]   Bauer, S. X., Krist, S. E., and Compton, W. B. "Generation of the Ares I-X Flight Test Vehicle Aerodynamic Data Book and Comparison to Flight," AIAA Paper 2011–0011.

[10] Abdol-Hamid, K. S., Ghaffari, F., and Parlette, E. B., "Ares I Vehicle Computed Turbulent Ascent Aerodynamic Data Development and Analysis," *Journal of Spacecraft and Rockets*, Vol. 49, No. 4, 2012, pp. 596-608.

[11] Warwick, G., "Lockheed Martin Refines Hybrid Wing-Body Airlifter Concept," Aviation Week & Space Technology, February 17, 2014, p.40.

[12] Wick, A. T., Hooker, J. R., and Zeune, C. H., "Integrated Aerodynamic Benefits of Distributed Propulsion," AIAA Paper 2015-1500.

[13] Hooker, J. R., Wick, A., Zeune, C., and Agelastos, A., "Over Wing Nacelle Installations for Improved Energy Efficiency," AIAA Paper 2103-2920.

[14] Pandya, M. J., Frink, N. T., Ding, E., and Parlette, E. B., "Toward Verification of USM3D Extensions for Mixed Element Grids," AIAA Paper 2013-2541.

[15] Pandya, M. J., Diskin, B., Thomas, J. L., and Frink, N. T., "Improved Convergence and Robustness of USM3D Solutions on Mixed Element Grids," *AIAA Journal*, Vol. 54, No. 9, 2016, pp 2589-2610.

[16] Pandya, M. J., Diskin, B., Thomas, J. L., and Frink, N. T., "Assessment of USM3D Hierarchical Adaptive Nonlinear Iteration Method Preconditioners for Three-Dimensional Cases," *AIAA Journal*, Vol. 55, No. 10, 2017, pp 3409-3424.

[17] Pandya M. J., Jespersen D. C., Diskin B., Thomas J. L., and Frink N. T., "Accuracy, Scalability, and Efficiency of Mixed-Element USM3D for Benchmark Three-Dimensional Flows," AIAA Paper 2019-2333.

[18] Van Leer B., "Towards the ultimate conservative difference scheme. III. upstream-centered finite difference schemes for ideal compressible flow," *Journal of Computational Physics*, Vol. 23, pp. 263–275, 1977.

[19] Van Leer B., "Upwind-difference methods for aerodynamic problems governed by the Euler equations," *In Fluid Mechanics, Lectures in Applied Mathematics*, Vol. 22, pp. 327–335, 1985

[20] Anderson W. K., Thomas J. L., and van Leer B., "Comparison of Finite Volume Flux Vector Splittings for the Euler Equations," *AIAA Journal*, Vol. 24, No. 9, 1986, pp. 1453–1460.

[21] Burg, C. O. E., "Higher Order Variable Extrapolation for Unstructured Finite Volume RANS Flow Solvers," AIAA Paper 2005-4999.

[22] Mitchell, C. R., "Improved Reconstruction Schemes for the Navier-Stokes Equations on Unstructured Meshes," AIAA Paper 1994-0642.

[23] Frink, N. T., "Tetrahedral Unstructured Navier-Stokes Method for Turbulent Flows," *AIAA Journal*, Vol. 36, No. 11, 1998, pp. 1975-1982. doi: 10.2514/2.324

[24] Biedron R.T., Carlson J.-R., Derlaga J.M., Gnoffo P.A., Hammond D.P., Jones W.T., Kleb B., Lee-Rausch E.M., Nielsen E.J., Park M.A., Rumsey C.L., Thomas J.L., Thompson K.B., and Wood W.A., "FUN3D Manual: 13.6," NASA TM 2019-220416, 2019.

[25] Nielsen, E. J., and Diskin, B., "High-Performance Aerodynamic Computations for Aerospace Applications," *Parallel Computing*, Vol. 64, 2017, pp. 20–32.

[26] Walden A., Nielsen E.J, Diskin B., and Zubair M., "A Mixed Precision Multicolor Point-Implicit Solver for Unstructured Grids on GPUs," 2019 IEEE/ACM 9th Workshop on Irregular Applications: Architectures and Algorithms (IA3), Denver, CO, USA, 2019, pp. 23-30. DOI: 10.1109/IA349570.2019.00010

[27] William K. Anderson, Newman J.C. and Karman S.L., "Stabilized Finite Elements in FUN3D," AIAA Paper 2017-0077.

[28] Derlaga J. M, Jackson C. W., and Buning P. G., "Recent Progress in OVERFLOW Convergence Improvements," AIAA Paper 2020–1045, 2020.

[29] Galbraith, M. C., Allmaras, S. R., and Darmofal, D. L., "SANS RANS Solutions for 3D Benchmark Configurations," AIAA Paper 2018–1570, 2018.

[30] Huang, A. C., "An Adaptive Variational Multiscale Method with Discontinuous Subscales for Aerodynamic Flows," Ph.D. thesis, Massachusetts Institute of Technology, Feb. 2020.

[31] Huang, A. C., Carson, H.A., Allmaras, S. R., Galbraith, M. C., Darmofal, D. L., and Kamenetskiy, D. S., "A Variational Multiscale Method with Discontinuous Subscales for Output-Based Adaptation of Aerodynamic Flows," AIAA Paper 2020-1563, 2020.

[32] Galbraith, M. C., Allmaras, S. R., and Darmofal, D. L., "A Verification Driven Process for Rapid Development of CFD Software," AIAA Paper 2015–818, 2015.

[33] Abhyankar, S., Brown, J., Constantinescu, E. M., Ghosh, D., Smith, B. F., and Zhang, H., "PETSc/TS: A Modern Scalable ODE/DAE Solver Library," *Computing Research Repository (CoRR)*,Vol.Numerical Analysis (math.NA),No. arXiv:1806.01437, 2018. URL http://arxiv.org/abs/1302.6066.

[34] Balay, S., Abhyankar, S., Adams, M. F., Brown, J., Brune, P., Buschelman, K., Dalcin, L., Eijkhout, V., Gropp, W. D., Kaushik, D., Knepley, M. G., McInnes, L. C., Rupp, K., Smith, B. F., Zampini, S., Zhang, H., and Zhang, H., "PETSc Users Manual," Tech. Rep. ANL-95/11 - Revision 3.8, Argonne National Laboratory, 2017.

[35] Balay, S., Gropp, W. D., McInnes, L. C., and Smith, B. F., "Efficient Management of Parallelism in Object Oriented Numerical Software Libraries," *Modern Software Tools in Scientific Computing*, edited by E. Arge, A. M. Bruaset, and H. P. Langtangen, Birkhäuser Press, 1997, pp. 163–202.

[36] Saad, Y., and Schultz, M. H., "GMRES: A Generalized Minimum Residual Algorithm for Solving Nonsymmetric Linear Systems," *SIAM Journal of Scientific and Statistical Computing*, Vol. 7, 1986, pp. 856–869.

[37] Diskin B., Thomas J. L., Rumsey C. L., and Pandya M. J., "Reference Solutions for Benchmark Three Dimensional Turbulent Flows," AIAA Paper 2016-0858.

[38] Gand, F., Deck, S., and Brunet, V., "Flow Dynamics Past a Simplified Wing Body Junction," *Physics of Fluids*, Vol. 22, No. 11, 2010, pp. 11511, doi: https://doi.org/10.1063/1.3500697.

[39] Bordji, M., Gand, F., Deck, S., and Brunet, V., "Investigation of a Nonlinear Reynolds-Averaged Navier-Stokes Closure for Corner Flows," *AIAA Journal*, Vol. 54, No. 2, 2016, pp. 386–398, doi: https://doi.org/10.2514/1.J054313.

[40] Wood, D. H. and Westphal, R. V., "Measurements of the Flow around a Lifting-Wing/Body Junction," AIAA Journal, Vol. 30, No. 1, 1992, pp. 6–12, doi: https://doi.org/10.2514/3.10875.

[41] Rumsey, C. L., Carlson, J.-R., and Ahmad, N., "FUN3D Juncture Flow Computations Compared with Experimental Data," AIAA Paper 2019-0079.

[42] Lee, H. C. and Pulliam, T. H., "Overflow Juncture Flow Computations Compared with Experimental Data," AIAA Paper 2019-0080.

[43] Rumsey, C. L., Lee, H. C. and Pulliam, T. H., "Reynolds-Averaged Navier-Stokes Computations of the NASA Juncture Flow Model Using FUN3D and OVERFLOW," AIAA Paper 2020-1304.

[44] Abdol-Hamid K.S., N. N., Carlson J.-R., and R.T., "Juncture Flow Computations using kL-Based Turbulence Models," ," AIAA Paper 2020-1305

[45] Eisfeld B., Togiti V., Braun S. and Stuermer A. W., "Reynolds-Stress Model Computations of the NASA Juncture Flow Experiment," AIAA Paper 2020-1306

[46] Balin R., Wright J., Patterson J., Farnsworth J. A., Evans J. A., Lakhani R., Spalart P. and Jansen K. E., "Hybrid Turbulence Model Computations of the NASA Juncture Flow Model Using PHASTA," AIAA Paper 2020-1777

[47] Iyer P. S. and Malik M. R., "Wall-modeled LES of the NASA Juncture Flow Experiment," AIAA Paper 2020-1307

[48] Lozano-Duran A., Bose S. T., and Moin P., "Prediction of trailing edge separation on the NASA Juncture Flow using wall-modeled LES," AIAA Paper 2020-1776

[49] Duda B. M. and Laskowksi G. M., "Lattice-Boltzmann Very Large Eddy Simulations of the NASA Juncture Flow Model," AIAA Paper 2020-1778